Article:
Fukagai, S., Brunskill, H.P., Hunter, A.K. et al. (2 more authors) (2019) Transitions in rolling-sliding wheel/rail contact condition during running-in. Tribology International. ISSN 0301-679X

https://doi.org/10.1016/j.triboint.2019.03.037

Transitions in rolling-sliding wheel/rail contact condition during running-in

S. Fukagai[a,b,*], H. P. Brunskill[a], A. K. Hunter[a], R. S. Dwyer-Joyce[a], R. Lewis[a]

[a] *The Leonardo Centre for Tribology, Department of Mechanical Engineering, University of Sheffield, Sheffield, UK*
[b] *Railway Technical Research Institute, Tokyo, Japan*

Abstract

The risk of wheel-climb derailment increases if the traction coefficient in the wheel/rail contact is too high. This has been observed to happen more frequently just after wheel machining. This work investigates how the traction coefficient rises with evolution of the wheel/rail interface during the running-in. Experiments were performed using a full-scale wheel/rail contact rig and an ultrasonic array transducer mounted in the rail. Results were used to determine the stiffness of the contact interface. Contact stiffness appeared to be positively correlated with the traction coefficient. Owing to the conforming of the interface, contact stiffness increases before the traction coefficient rises. The work will allow recommendation of wheel machining to be made to help reduce the problem of wheel-climb derailment.

Keywords: rolling-sliding; ultrasound; contact stiffness; traction coefficient.

1. Introduction

Since the frictional condition between the wheel and rail plays a vital role in the transmission of driving force and braking force, it should be kept at an optimum level to secure the proper acceleration performance and braking distance. On the other hand, it is known that high traction coefficient and slip at curves could lead to severe wear and deformation of wheel and rail, energy consumption and squealing noise [1]. It also increases the risk of a wheel climb derailment occurring [2][3][4].

Nakahara *et al.* reported that the traction condition between a wheel and rail changes with a train traffic passage even in the dry condition [5] and showed some transient traction curves using twin-disk testing which indicated that traction coefficient varies with the evolution of surface roughness during running-in [6]. Blau also addressed the tribological behaviour during running-in and reported typical examples of friction force transition curves [7]. Notedly, it was mentioned that the friction force tends to increase significantly in the case of dry contact after the start of sliding contact. In these cases, it is commonly recognized that one of the main causes for such a transition is the evolution

*Corresponding author.
Email address: fukagai.shinya.81@rtri.or.jp (Shinya Fukagai)

of surface topography with cyclic contacts [6][7]. Lundmark *et al.* [8] and Yamamoto and Chen [9][10] also reported that the transitions in traction coefficient are strongly influenced by the initial topography.

A railway wheel experiences re-profiling several times during its whole life to reset it to the designed profile from the worn profile or to remove damage, such as wheel flat and cracks. And it is known that some derailments have occurred relatively soon after re-profiling of wheels [11][12][13][14]. Just after re-profiling, the wheel surface has a large roughness which is caused by the machining marks. Some reports mention the possibility that the rougher surface leads to a higher traction coefficient, and so increases the risk of flange climb derailment [13][14][15]. Specifically, they indicate that the spike-like machining marks cause an increase in traction during running-in as they plough into the rail material. Therefore, a smooth surface is recommended at the finishing of wheel machining [13][15]. On the other hand, there is another opinion that traction force is increased with the deformation of machining marks and increase in real contact area [11]. As the wheel and rail experience cyclic rolling-sliding with tangential force, the surface topography changes and therefore the interfacial condition alters dramatically during running-in. Therefore, it is important to understand how this interfacial condition evolves over time to understand the potential mechanisms for wheel climb derailment. However, the difficulty in obtaining accurate non-destructive interfacial measurements has hindered systematic experimental investigations. An increased understanding of these effects might inform rail service providers about optimal wheel profiling methods and lubrication programs to reduce the likelihood of wheel climb derailment.

Pressure-sensitive films can be used to observe contact area and stress in a static contact. However, these films can cause over-prediction of the contact area owing to the thickness of the film and changes in tangential force due to its different frictional properties. Practical implementation is also difficult because the film disintegrates under the high-pressure and shear between the wheel and the rail. Recently, ultrasonic techniques have been used to observe the contact between wheel and rail [16][17][18][19][20]. Though there are spatial resolution limits and considerations of transducer positioning to ensure the sound waves reflect off the area of interest, this technique can be used to non-invasively and directly observe the contact. When an ultrasonic wave strikes the interface between the wheel and rail, it is partially transmitted and partially reflected. The proportion of the wave reflected depends on the stiffness of the contact [21][22]. This approach has been used to determine the contact pressure distribution in wheel-rail contacts and the influence of wear, roughness and surface defects on the contact patch [17][19]. This actual distribution of the contact pressure could apply to the simulation of wear amount and damage propagation with consideration for surface topography [23][24].

Recently, dynamic ultrasonic measurement of a rolling-sliding contact has been achieved [25][26]. Using this method, the dynamic contact in rolling-sliding can be obtained for repeated cycles. Information about the contact condition under the cyclic tangential force might lead to the clarification of mechanism about tribological transition curve during running-in.

The aim of this work was to understand and characterize the tribological behaviour between wheel and rail during running-in. Ultrasonic reflection was used to evaluate interface condition in a rolling-sliding contact, particularly contact stiffness over time as running-in occurs. The experiments were performed using a full-scale dynamic wheel/rail contact-testing machine and a 64 element ultrasonic array transducer

mounted in the rail. Transient traction coefficient was also measured during the test. Following these measurements, a comparison between contact stiffness and traction coefficient was carried out.

2. Methodology

2.1. Full-scale dynamic wheel/rail rig

Figure 1 shows a schematic diagram of the full-scale dynamic wheel/rail contact rig [25][27], which was equipped with a full−scale wheel loaded onto a traversing rail. It could apply a normal force of up to 200 kN and tangential force of up to 60 kN using servo-controlled hydraulic cylinders. The rail was pushed and pulled at a velocity of up to 100 mm/s in the longitudinal direction. The wheel could be unconstrained so that its rotation was a result of the friction force between the wheel and the rail, and it could also be forced to rotate slightly faster by the movement of an actuator which was connected to it via a chain. The difference in speed generated the tangential force. Each hydraulic cylinder had a load cell mounted in-line facilitating the measurement of traction coefficient from the division of tangential force by normal force.

[Figure 1 about here.]

Figure 2 shows a photograph of the ultrasonic array transducer and a schematic of the set-up. The transducer was mounted in a hole that was made in the rail in the direction parallel to the sleeper. Hence, the contact area could be scanned with the passage of the wheel on the rail where the transducer was mounted. The array transducer consisted of 64 piezo elements arranged linearly each with a width of 0.5 mm and a constant pitch of 0.6mm. The sampling interval in the rolling direction was determined by the ultrasonic array scanning frequency and the wheel rolling velocity. Since the scanning frequency was approximately 14 Hz and the rolling speed for these tests was 10 mm/s, the sampling interval in the rolling direction was approximately 0.7 mm. The frequency of the ultrasound was 5 MHz.

[Figure 2 about here.]

2.2. Ultrasound technique

At an interface of two dissimilar materials, part of the incident ultrasonic wave is transmitted through the interface and the other part is reflected. For an interface of two dissimilar materials perfectly bonded, the proportion of the reflected wave, described by the reflection coefficient R, is dependent on the acoustic impedance mismatch between the two materials and is given by [28]:

$$R = \frac{z_2 - z_1}{z_2 + z_1} \tag{2}$$

where z_1 and z_2 are the acoustic impedances (which are the products of density and acoustic velocity) of the contacting materials. Therefore, for two perfectly bonded identical materials, the interface would have no reflection (z_1=z_2, R=0) and the entire wave is transmitted (without any losses). Conversely, an ultrasonic wave is almost completely reflected at an interface between two materials with substantially different acoustic impedances, as in the case of a solid and a gas (R≈1).

Real engineering interfaces are inherently rough and micro and macroscopic air gaps are

formed at an interface. Presuming the length of the ultrasonic wave is long relatively to the size of the air gaps the whole interface behaves as a single reflector and therefore R is also dependent on the contact stiffness of the interface [21][22]. The contact stiffness, K, is a function of the surface topography, surface material properties and the contact pressure and has a significant influence on the contact dynamics. As the surface topography changes due to elastic and plastic deformation, the measured reflection coefficient R will change accordingly as shown in Fig. 3. The contact stiffness could vary from zero for a pair of surfaces just in contact to infinity when they are perfectly bonded. In principle, the degree of conformity at the interface can be determined by measuring the reflection coefficient of the ultrasonic wave.

[Figure 3 about here.]

Tattersall [22] used an interface 'spring model' to show how the reflection coefficient is related to contact stiffness:

$$R = \frac{z_1 - z_2 + i\omega(z_1 z_2/K)}{z_1 + z_2 + i\omega(z_1 z_2/K)} \tag{2}$$

where ω is the angular frequency of the ultrasound and K is the interfacial contact stiffness. The contact stiffness is defined as the stiffness due to asperity contact per unit area of an interface, as shown in following equation.

$$K = -\frac{dp}{du} \tag{3}$$

where p is the nominal contact pressure and u is the distance between the surface mean lines. In the case of present work, the materials on both sides of the interface are similar (z_1=z_2=z), then equation (2) reduces to:

$$|R| = \frac{1}{\sqrt{1 + (2K/\omega z)^2}} \tag{4}$$

Therefore, if the reflection coefficient, R, can be experimentally obtained, the contact stiffness, K can be estimated. Generally, normal contact stiffness can be distinguished from shear contact stiffness depending on the loading direction. The contact stiffness in this paper means the normal contact stiffness unless otherwise specified.

Many researchers [16][17][18][19][20] have obtained the reflection coefficient R as the ratio of the reflected ultrasonic wave amplitude under load, H, to that when unloaded with no material in contact, H_0 (the reference).

$$R = \frac{H}{H_0} \tag{5}$$

When unloaded, the contact is effectively steel against air and so the wave can be assumed

to be fully reflected and thus H_0 is equivalent to the incident wave amplitude. This is a simple practical way to obtain the reflection coefficient and removes the influence of transducer characteristics, ultrasonic wave scattering and attenuation.

2.3. Test rail and wheel

Figure 4 shows the profile of test rail and wheel which were measured using a non-contact profile measurement device (CW40, CALIPRI). The type of the test rail was UIC60A (EN 13674-1) at a length of 1200 mm and that of the test wheel was P8 (EN 13715) at a diameter of 920mm. Since the rail and the wheel were used for full-scale contact tests before this test, both had been slightly worn. There were two choices for contact location on the rail by inverting the direction of the rail in the rig. Two roughness conditions were prepared on each side of the rail (Fig. 4(a)). On one side, a rough surface topography was created by intentionally running the rig in a high traction force rolling-sliding condition. On the other side of the rail, the surface was prepared by polishing with sandpaper predominantly along the longitudinal direction to create a smoother surface. The contact location on the wheel was fixed (Fig. 4(b)) and the surface of the wheel was not specially prepared.

[Figure 4 about here.]

Silicon polymer replicas (Microset 101 Fluid and NP10 Nozzle) were used to copy the surface topography of rail and wheel. After obtaining the replica, the roughness and surface topography were analyzed using an optical surface measurement system (InfiniteFocus, Alicona). Figure 5 shows the initial surface profile of rail and wheel for each case. The plus and minus sign of these profiles have been reversed to be same as the actual surface because the profiles were obtained from the replica. The measurements were carried out five times per direction, lateral and tangential. Table 1 shows initial roughness value of rail and wheel which is the mean value of five measurements. It can be seen that the magnitude of rail roughness in rougher case is significantly larger than that in the smoother case. On the other hand, the magnitude of wheel roughness in rougher case is slightly smaller than that in smoother case. However, there was not a significant difference like the rail roughness. As a consequence, two combinations of the rail surface and the wheel surface which have different initial roughness were prepared.

[Figure 5 about here.]
[Table 1 about here.]

2.4. Test procedure

Table 2 shows the test conditions. The cyclic contact tests were continued up to 100 cycles in the test of the rougher case and 60 cycles in the smoother case. Both tests were carried out after cleaning the surface with acetone. The measurement of traction coefficient and reflection coefficient were carried out continuously during the cyclic tests. Silicon polymer replicas were used for the evaluation of roughness as mentioned in section 2.3. These replicas were obtained after 100 cycles in the test of the rougher case and after 20 cycles in the test of the smoother case when the increase of traction coefficient showed saturation with the increase of cycles. The velocity was quite low, 10 mm/sec. Though it is well known that the traction coefficient is influenced by the velocity when fluid, such as water, gets in between the wheel and the rail, this influence is small in the dry condition[29].

[Table 2 about here.]

3. Results

3.1. Change of traction coefficient with cyclic rolling

Figure 6 shows the relationship between the number of cycles and the traction coefficient. Traction coefficient was calculated as the ratio of tangential force to drive the wheel and the normal force (Fig. 1) and the value was extracted at the moment the wheel passed the ultrasonic transducer. Both results of the rougher case and the smoother case showed the increase of traction coefficient with the increase in cycles and it is clearly found that the increase in the smoother case was more rapid than that of the rougher case. In both cases, the traction coefficient reached a plateau of approximately 0.5.

[Figure 6 about here.]

3.2. Change of contact stiffness with cyclic rolling

Reflection coefficient measurements were made continuously during the rolling cycles. The contact stiffness was determined from the measurements using equation (3). Figure 7 shows the contact stiffness maps between wheel and rail for different number of cycles. Here the threshold value of contact stiffness to define the contact area was determined as the value which was calculated by a 10% decrease of reflection coefficient (R=0.9). The threshold value of reflection coefficient was changed step-by-step and the largest value which doesn't contain appreciable background noise was found by comparison of the shape of contact area. The increase of contact stiffness with the increase in cycles can be seen in the change of contours. As the cycles progress, the surfaces are becoming more conformal.

[Figure 7 about here.]

Figure 8 shows a cross–section through contact stiffness maps. Here, each line was selected to pass through the point which had the maximum contact stiffness. It was found that the increasing tendency is not uniform inside the contact area and there were some peak points that showed a significant increase for both rougher and smoother cases. It is thought that the region of higher contact pressure generates more significant evolution of contact interface.

[Figure 8 about here.]

Figure 9 shows the relationship between the mean contact stiffness and the number of cycles. Here, the mean value was calculated using the data which exceeded the threshold value above mentioned. The mean contact stiffness increased with the cyclic rolling and the value of the smoother case saturated more rapidly than that of the rougher case. This tendency was similar to the transition of traction coefficient.

[Figure 9 about here.]

3.3. Change of surface topography with cyclic rolling

Figure 10 shows a comparison of the surface topography before and after test cycles. Here, it should be noted that what appears to be a projection is actually a dent because these images were obtained from a replica. Figure 10 (a) shows that the initial asperities on the rail in the rougher case were flattened dramatically. Fig. 10 (b) and (d) at the wheel after test cycles showed the evolution of stripe-like traces along with the traction force. It is thought that the traction force makes such traces.

[Figure 10 about here.]

Figure 11 shows a comparison of the profiles before and after the test cycles. The measurement of profiles was carried out in a similar way to that described in section 2.3. Figure 11 (a) shows that the initial asperities on the rail in the rougher case were flattened dramatically. On the other hand, Fig. 11 (b) shows that the roughness on the wheel in the rougher case slightly increased after the cycles. It is thought that this increase was due to compressions by the asperity summits of the rail surface or the surface texturing by the traction force. Figure 11 (c) and (d) show that there was no significant difference before and after the cycles.

[Figure 11 about here.]

Figure 12 shows the comparison of root-mean-square roughness value (Rq) for each case, rail/wheel and directions. Here, these were mean values for five measurements and the error bar means the range from maximum value to minimum value, which is the same as the actual surface (reverse value of replica). Figure 12 (a) shows that Rq of rail in the rougher case dramatically decreased and Fig. 12 (b) shows that Rq of wheel in the rougher case slightly increased after the cyclic tests in the rougher case. Figure 12 (c) and (d) show that there was no significant difference before and after the cycles in the smoother case.

[Figure 12 about here.]

4. Discussion

The continuous evaluation of contact stiffness during the running-in period revealed that contact stiffness increases with an increase in cycles. However, the tendencies of increase differed from the rougher case to the smoother case. The increase of contact stiffness in the rougher case can be explained by the significant decrease in rail roughness. As the roughness reduces, the surface conforms more and the stiffness increases. Though there was also an increase of contact stiffness in the smoother case, there was no significant change in roughness value. However, the tops of asperities produce geometrical conformity on the sub-microscale, even though they have not led to a significant decrease in root-mean-square roughness value.

For a more detailed analysis of surface topography, additional parameters, skewness (Rsk) and kurtosis (Rku) were evaluated. Figure 13 shows a schematic illustration of surface topography with ranging skewness and kurtosis [30]. Skewness is the parameter to evaluate the symmetry of the roughness profile [30][31]. A zero value of Rsk means a symmetrical distribution, a negative value means the profile has an inclined distribution in the upper side of a mean line and a positive value means the profile has an inclined distribution in the lower side of a mean line. Kurtosis is the parameter to evaluate the sharpness of asperity summits of the roughness profile [30][31]. If Rku is smaller than three, it means there is a platykurtic distribution and if the value is larger than three, it means there is a leptokurtic distribution.

[Figure 13 about here.]

Figure 14 (a) and (b) show the comparison for skewness (Rsk) of the profile which was shown in Fig. 11. In the smoother case, there is a relatively large increase in the lateral direction of the rail before the test to after 20 cycles. Figure 14 (c) and (d) show the comparison of kurtosis (Rku) of the profile which was shown in Fig. 11. In the smoother case, there is a noticeable difference in the lateral direction on the rail before the test to after 20 cycles. Generally, a grinding process produces grooved surfaces with negative skewness but high kurtosis values [30]. Since the rail in the smoother case was prepared by polishing using sandpaper, it is reasonable that a negative Rsk value and large Rku value appeared before the test. It is thought that sharp scratching marks were deformed during the running-in period and the change of roughness distribution showed the difference in Rsk and Rku after the cyclic test even if the Rq was almost the same. Therefore, this change should have caused the slight increase of contact stiffness in the smoother case.

[Figure 14 about here.]

Figure 15 shows the relationship between mean contact stiffness and traction coefficient. The mean contact stiffness in the rougher case appears to have a positive correlation with the traction coefficient and is close to being linear. On the other hand, the relationship in the smoother case was relatively skewed and the traction coefficient is much less dependent on contact stiffness. Contact stiffness is an effect dominated by roughness and deformation under load, while the traction coefficient is much more dependent on surface conditions and contamination, such as water and oxide layer. In the smoother case, the surface condition influences the traction more strongly than the rougher case. It is thought that these influences decreased with the increase of the cyclic number and the wear of outer surface

layer.

[Figure 15 about here.]

Figure 16 shows a schematic model of the transition of surface roughness and contact stiffness. Here, it is simplified as the contact between a completely flat surface and a rough surface. As mentioned in section 2.2, normal contact stiffness can be distinguished from shear contact stiffness depending on the loading direction. Normal contact stiffness increases with the increase of cyclic rolling-sliding contacts and the decrease of roughness. There are several studies which discuss how shear contact stiffness increases with the increase of normal contact stiffness and the ratio of shear stiffness to normal stiffness is nearly constant as a function of Poisson's ratio [32][33][34]. The displacement along the tangential direction, Δx, would be qualitatively dominated by the slip ratio and it was constant, three percent, during this test. Therefore, it is thought that the shear stress increased with the increase of normal contact stiffness as the following equation:

$$\tau = cK \cdot \Delta x \tag{6}$$

where τ is shear stress and c is the ratio of shear stiffness to normal stiffness. As a consequence, there would be the linear-like relationship between normal contact stiffness and traction coefficient.

[Figure 16 about here.]

From this relationship, the reason why the traction coefficient under the smoother surface was larger is thought as the contact stiffness (the contact pressure to cause deformation of surface asperity) in the smoother case is larger than that in rougher case.

A smooth surface is sometimes recommended at the finishing of wheel machining, because it is believed that the initial surface asperities cause a high traction coefficient by the spike-like effect. However, this paper revealed that the traction coefficient in the rougher case is smaller than the smoother case, because the contact stiffness is smaller. The plastic deformation of the asperities with the cyclic rolling-sliding makes the contact stiffness larger and it will settle in a similar value after the running-in.

It has already been found that the contact stiffness is affected by the contact pressure. Therefore, the effect of contact pressure should be taken into account for the direct estimation of the traction force/acceleration force using the contact stiffness and it will be a future work.

Oxides will be generated in the contact during testing, but there are currently no real time methods for assessing this that would enable the layer to be related to friction. Post-test analysis[35] has shown that the ex-situ layers from testing are thicker than those on actual rail which may be significant, but more work would be needed to investigate this.

5. Conclusions

From the measurement of rolling-sliding contact condition between wheel and rail using ultrasound waves, the following conclusions can be drawn:

1. Both the rougher case and the smoother case showed an increase in traction coefficient with the increase of cycles and it is clearly found that the increase in the smoother case was more rapid than that of the rougher case.
2. Mean contact stiffness which was measured using ultrasonic waves increased with the cyclic rolling and the value of the smoother case saturated more rapidly than that of the rougher case. This tendency was similar to the transition of traction coefficient.
3. Root-mean-square roughness in the rougher case showed that the initial asperity was flattened dramatically after the cyclic rolling-sliding. Though that in the smoother case showed no significant change, there was an increase in skewness and a decrease of kurtosis.
4. Mean contact stiffness appears to have a positive correlation with the traction coefficient and is close to being linear. Based on the above results, a mechanism model of the effects of contact stiffness on traction characteristics during the running-in period was proposed.

Acknowledgements

R. S. Dwyer-Joyce, A. K. Hunter, and H. P. Brunskill would like to acknowledge the financial support of the Engineering and Physical Sciences Research Council for funding this research through the fellowship on Tribo-Acoustic Sensors EP/N016483/1.

References

[1] Lewis R, Olofsson U. Wheel-rail interface handbook. Elsevier; 2009.

[2] Shust WC, Elkins JA. Wheel forces during flange climb part I - track loading vehicle tests. Railr. Conf. 1997., Proc. 1997 IEEE/ASME Joint., 1997, p. 137–47.

[3] Ishida H, Miyamoto T, Maebashi E, Doi H, Iida K, Furukawa A. Safety Assessment for Flange Climb Derailment of Trains Running at Low Speeds on Sharp Curves. Q Rep RTRI 2006;47:65–71. doi:10.2219/rtriqr.47.65.

[4] Matsumoto A, Sato Y, Ohno H, Tomeoka M, Matsumoto K, Kurihara J, et al. A new measuring method of wheel-rail contact forces and related considerations. Wear 2008;265:1518–25. doi:10.1016/j.wear.2008.02.031.

[5] Nakahara T, Baek KS, Chen H, Ishida M. Relationship between surface oxide layer and transient traction characteristics for two steel rollers under unlubricated and water lubricated conditions. Wear 2011;271:25–31. doi:10.1016/j.wear.2010.10.030.

[6] Baek KS, Kyogoku K, Nakahara T. An experimental study of transient traction characteristics between rail and wheel under low slip and low speed conditions. Wear 2008;265:1417–24. doi:10.1016/j.wear.2008.02.044.

[7] Blau PJ. On the nature of running-in. Tribol Int 2005;38:1007–12. doi:10.1016/J.TRIBOINT.2005.07.020.

[8] Lundmark J, Kassfeldt E, Hardell J, Prakash B. The influence of initial surface topography on tribological performance of the wheel/rail interface during rolling/sliding conditions. Proc Inst Mech Eng Part F J Rail Rapid Transit 2009;223:181–7. doi:10.1243/09544097JRRT223.

[9] Yamamoto D, Chen H. A Fundamental Study on Fine Unevenness and Tangent Force on Wheel Tread of Railway Vehicle (Relations between Environmental Condition and Tangent Force Characteristics with a Two-Disk Rolling Machine). Trans JAPAN Soc Mech Eng Ser C 2011;77:3211–22. doi:10.1299/kikaic.77.3211.

[10] Yamamoto D, Chen H. Influence of the fine unevenness of wheel tread on the running stability of railway vehicle. Trans JAPAN Soc Mech Eng Ser C 2013;79. doi:10.1299/kikaic.79.2338.

[11] Doi H, Miyamoto T, Suzumura J, Nakahashi J, Chen H, Ban T. Change in Surface Condition of T urned Wheel and Effectiveness of Lubrication Turned against Flange Climb Derailment. Q Rep RTRI 2012;53:70–6.

[12] Kataori A, Doi K, Iijima H, Momosaki S, Matsumoto S. The Influence of the Wheel/Rail Contact Point Condition on Friction Coefficient. 9th World Conf Railw Res 2011.

[13] Greene S, Cook G, Ford NP, Freeland RL, Gilliam FM, Hough J a, et al. Flange Climb Derailment criteria and Wheel/Rail Profile management and Maintenance Guidelines for Transit Operations. vol. 5. 2005.

[14] Iwnicki S. Handbook of railway vehicle dynamics. CRC press; 2006.

[15] Stow J, Allen P. A Good Practice Guide for Managing the Wheel-Rail Interface of Light Rail and Tramway Systems. Off Rail Regul 2008.

[16] Pau M. Estimation of real contact area in a wheel-rail system by means of ultrasonic

waves. Tribol Int 2003;36:687–90. doi:10.1016/S0301-679X(03)00014-8.

[17] Marshall MB, Lewis R, Dwyer-Joyce RS, Olofsson U, Björklund S. Experimental Characterization of Wheel-Rail Contact Patch Evolution. J Tribol 2006;128:493–503. doi:10.1115/1.2197523.

[18] Dwyer-Joyce RS, Yao C, Zhang J, Lewis R, Drinkwater BW. Feasibility Study for Real Time Measurement of Wheel-Rail Contact Using an Ultrasonic Array. J Tribol 2009;131:041401. doi:10.1115/1.3176992.

[19] Pau M, Leban B. Ultrasonic assessment of wheel-rail contact evolution exposed to artificially induced wear. Proc Inst Mech Eng Part F J Rail Rapid Transit 2009;223:353–64. doi:10.1243/09544097JRRT241.

[20] Dwyer-Joyce RS, Yao C, Lewis R, Brunskill H. An ultrasonic sensor for monitoring wheel flange/rail gauge corner contact. Proc Inst Mech Eng Part F J Rail Rapid Transit 2013;227:188–95. doi:10.1177/0954409712460986.

[21] Kendall K, Tabor D. An Ultrasonic Study of the Area of Contact between Stationary and Sliding Surfaces. Proc R Soc A Math Phys Eng Sci 1971;323:321–40. doi:10.1098/rspa.1971.0108.

[22] Tattersall HG. The ultrasonic pulse-echo technique as applied to adhesion testing. J Phys D Appl Phys 1973;6:819–32.

[23] Rovira A, Roda A, Marshall MB, Brunskill H, Lewis R. Experimental and numerical modelling of wheel-rail contact and wear. Wear 2011;271:911–24. doi:10.1016/j.wear.2011.03.024.

[24] Pau M, Leban B, Guagliano M. Propagation of Sub-surface Cracks in Railway Wheels for Wear-induced Conformal Contacts. J Mech Syst Transp Logist 2010;3:226–35. doi:10.1299/jmtl.3.226.

[25] Zhou L, Brunskill H, Lewis R, Pletz M, Daves W, Scheriau S. Real time Measurement of Dynamic Wheel-Rail Contacts Using Ultrasonic Reflectometry. Submitt to J Tribol 2018.

[26] Brunskill HP. The Real-Time Characterisation of Dry Machine Element Contacts Using Ultrasonic Reflectometry. Ph.D. thesis, University of Sheffield, 2013.

[27] Lewis SR, Riley S, Fletcher DI, Lewis R. Optimisation of a railway sanding system for optimal grain entrainment into the wheel–rail contact. Proc Inst Mech Eng Part F J Rail Rapid Transit 2018;232:43–62. doi:10.1177/0954409716656220.

[28] Schoenberg M. Elastic wave behavior across linear slip interfaces. J Acoust Soc Am 1980;68:1516–21. doi:10.1121/1.385077.

[29] Ohyama T. Tribological studies on adhesion phenomena between wheel and rail at high speeds. Wear 1991;144:263–75.

[30] Bhushan B. Principles and applications to tribology. John Wiley & Sons; 1999.

[31] Gadelmawla ES, Koura MM, Maksoud TMA, Elewa IM, Soliman HH. Roughness parameters. J Mater Process Technol 2002;123:133–45. doi:10.1016/S0924-0136(02)00060-2.

[32] Sherif HA, Kossa SS. Relationship between normal and tangential contact stiffness of nominally flat surfaces. Wear 1991;151:49–62. doi:10.1016/0043-1648(91)90345-

U.

[33] Królikowski J, Szczepek J. Assessment of tangential and normal stiffness of contact between rough surfaces using ultrasonic method. Wear 1993;160:253–8. doi:10.1016/0043-1648(93)90428-O.

[34] Dwyer-Joyce RS, Gonzalez-Valadez M. Ultrasonic Determination of Normal and Shear Interface Stiffness and the Effect of Poisson' s Ratio. Transient Process Tribol 2004:143–9.

[35] Meierhofer A, Hardwick C, Lewis R, Six K, Dietmaier P. Third body layer-experimental results and a model describing its influence on the traction coefficient. Wear 2014;314:148–54. doi:10.1016/j.wear.2013.11.040.

List of Figures

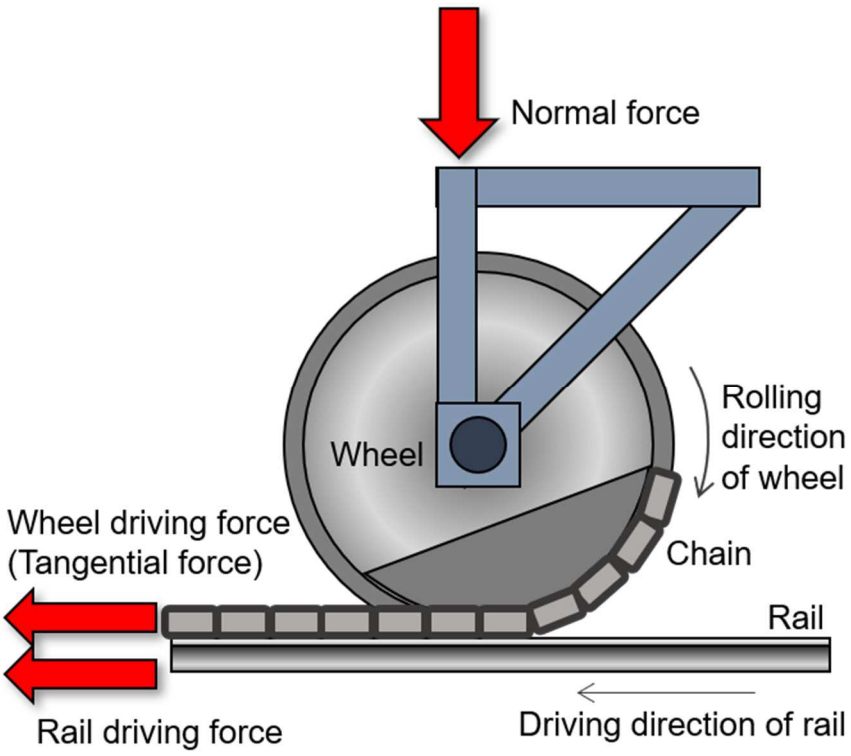

Figure 1. Schematic diagram of the full-scale dynamic wheel/rail contact rig.

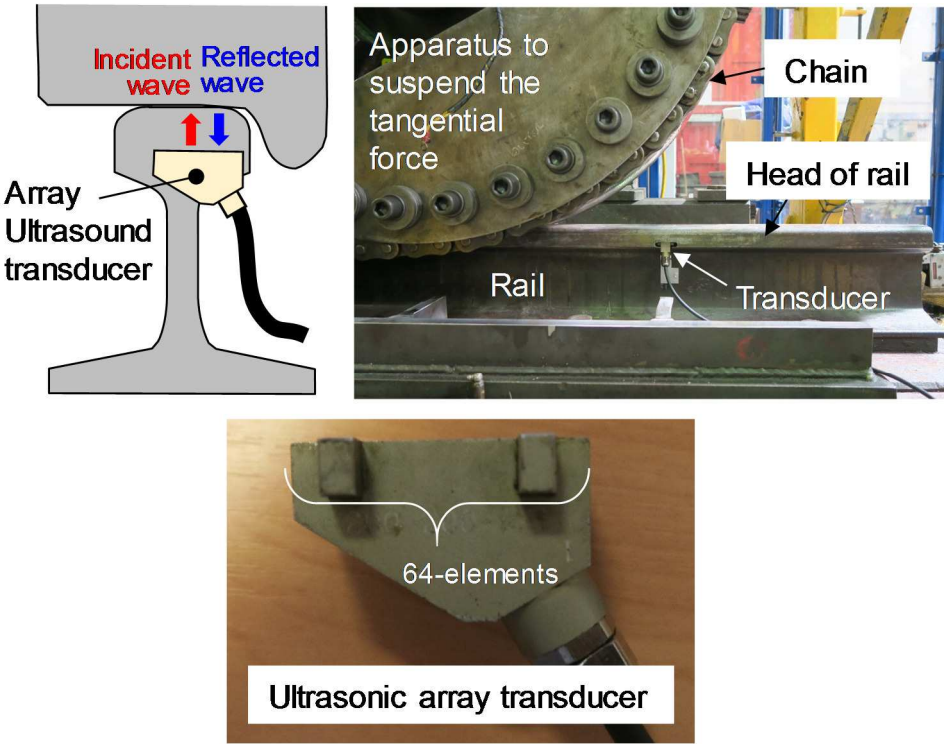

Figure 2. Ultrasonic array transducer and schematic of the set-up.

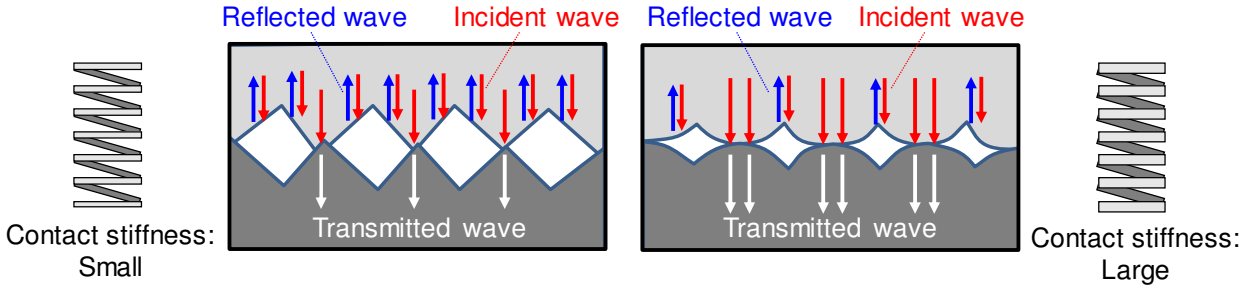

Figure 3. Principle of measurement.

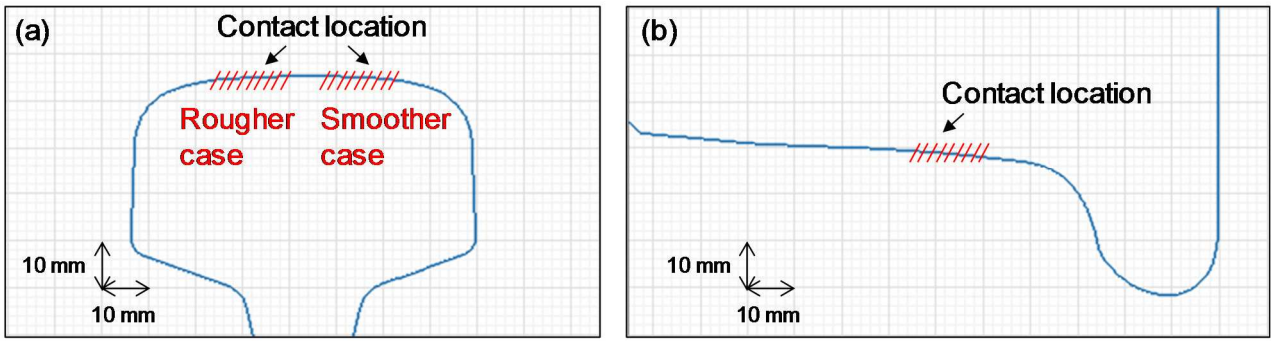

Figure 4. Measured profile of test rail and wheel and contact location, (a) rail, (b) wheel.

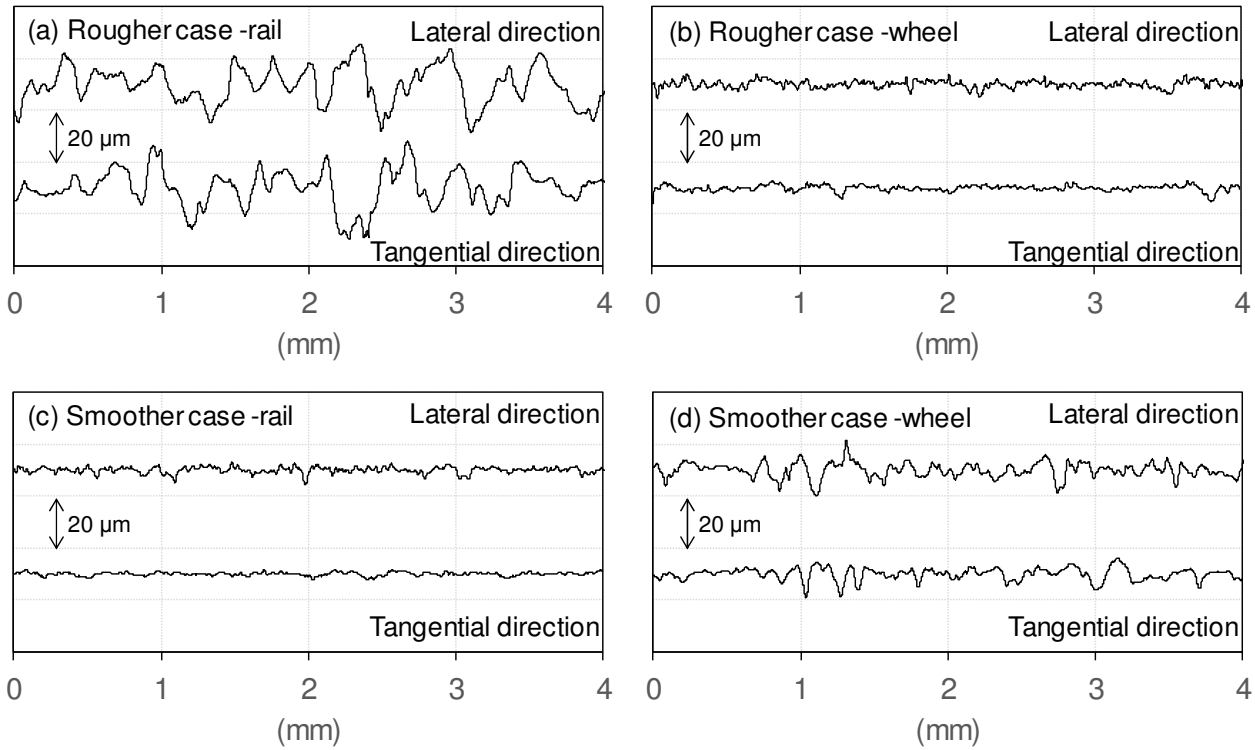

Figure 5. Initial roughness profile of rail and wheel for each test, (a) Rougher case - rail, (b) Rougher case-wheel, (c) Smoother case-rail, (d) Smoother case-wheel.

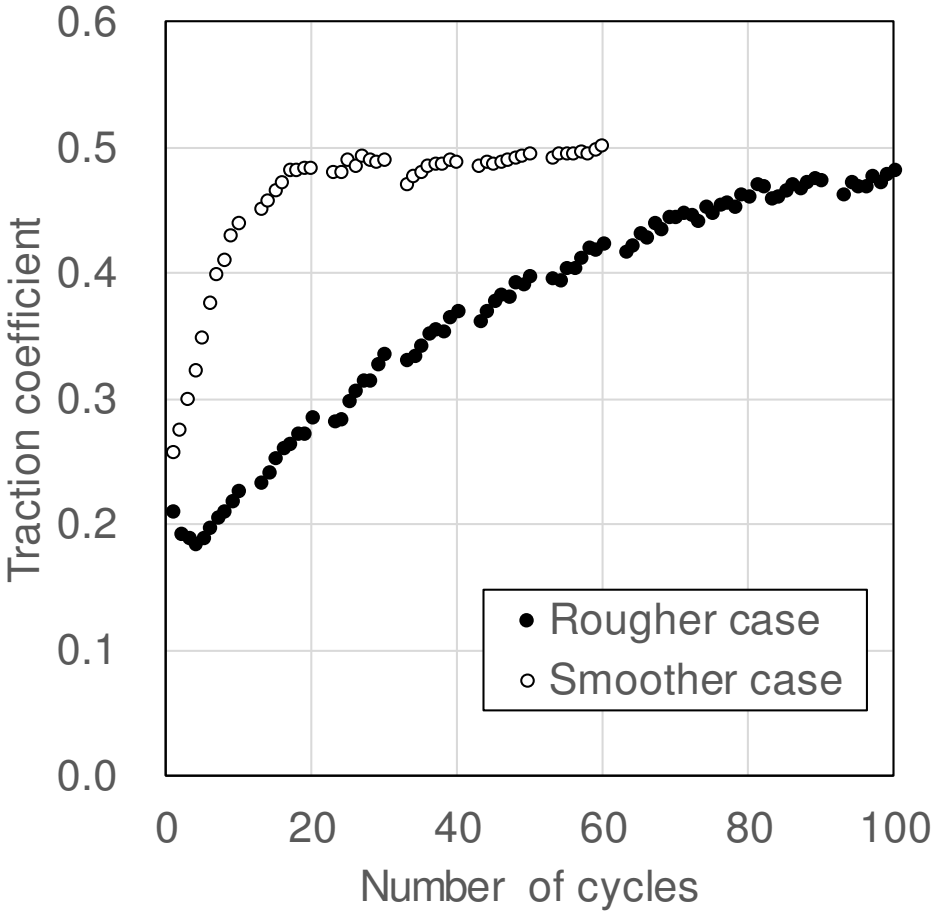

Figure 6. Relationship between number of cycles and traction coefficient.

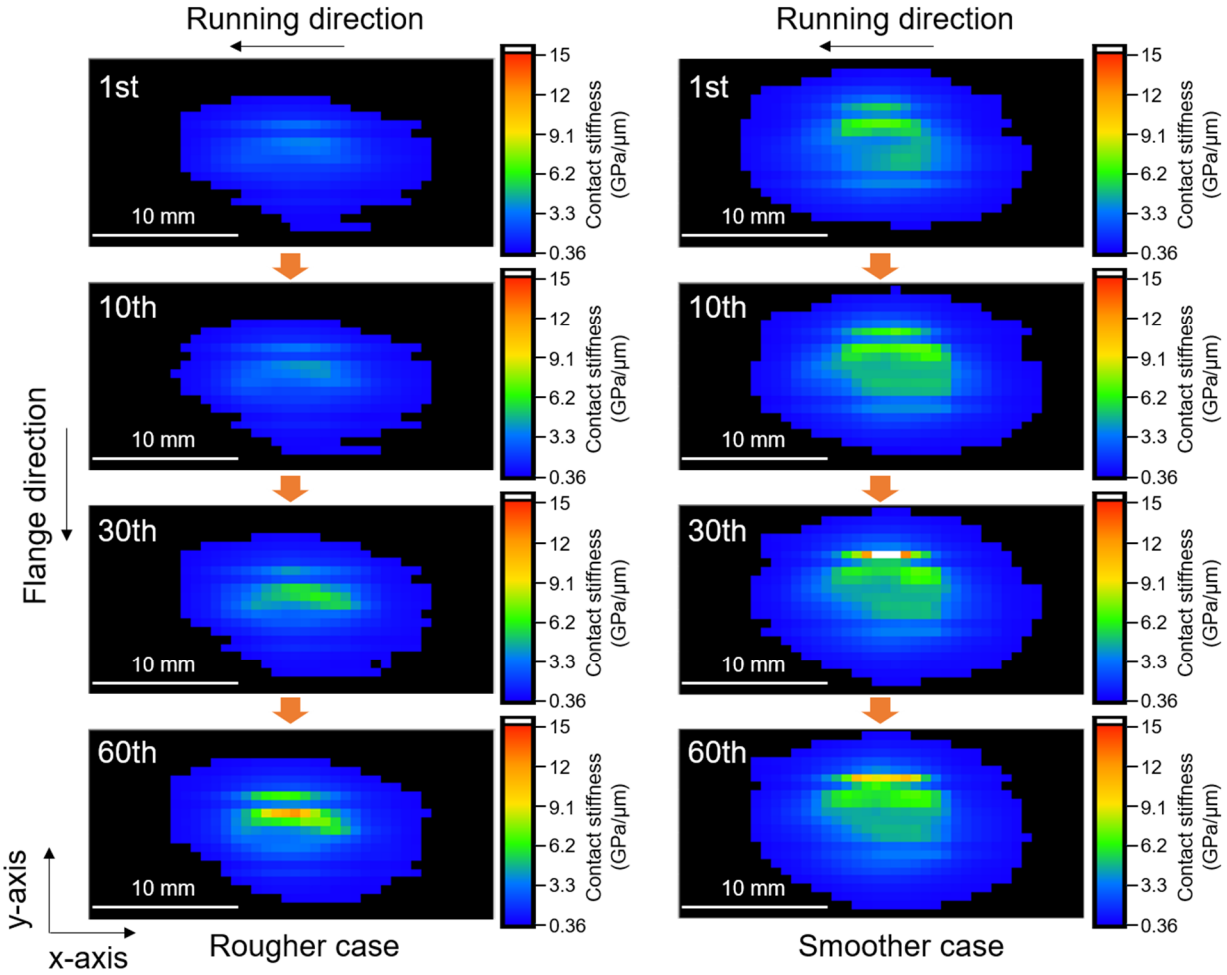

Figure 7. Contact stiffness maps between wheel and rail for different number of cycles.

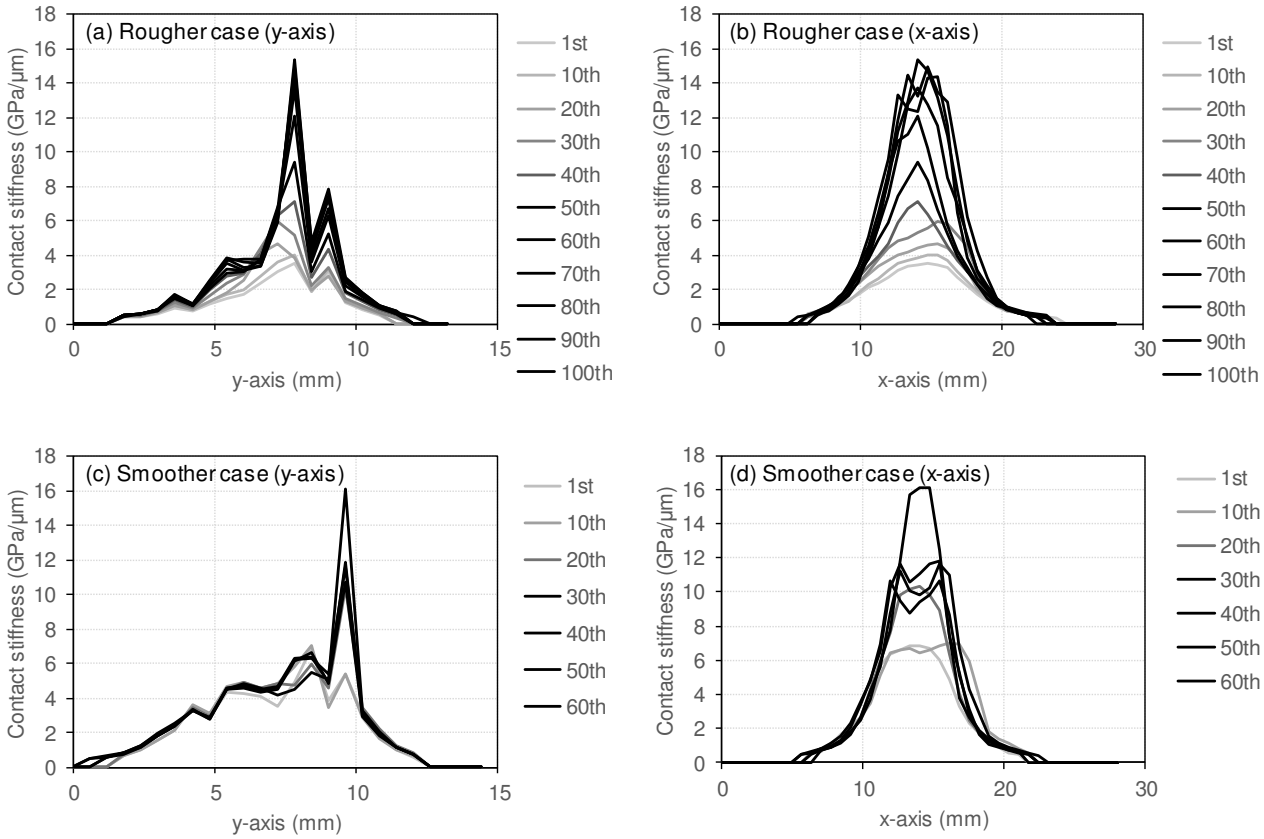

Figure 8. Cross-section through contact stiffness maps, (a) Rougher case along the y-axis, (b) Rougher case along the x-axis, (c) Smoother case along the y-axis, (d) Smoother case along the x-axis.

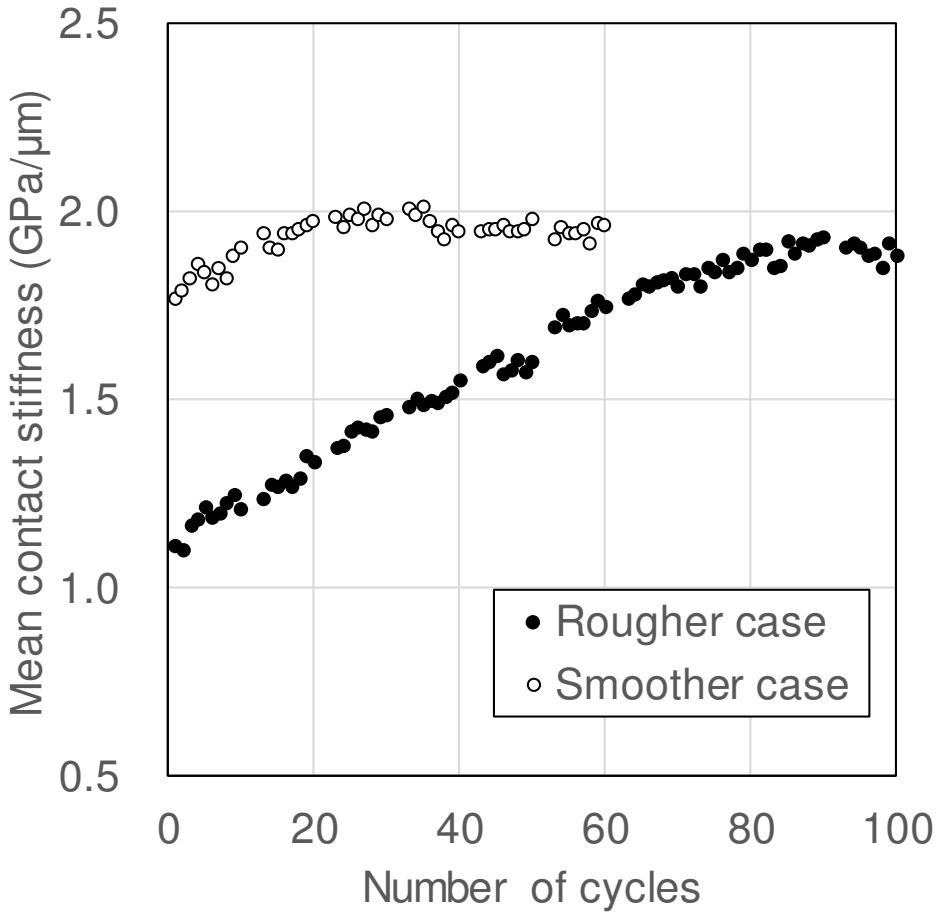

Figure 9. Relationship between number of cycles and mean contact stiffness.

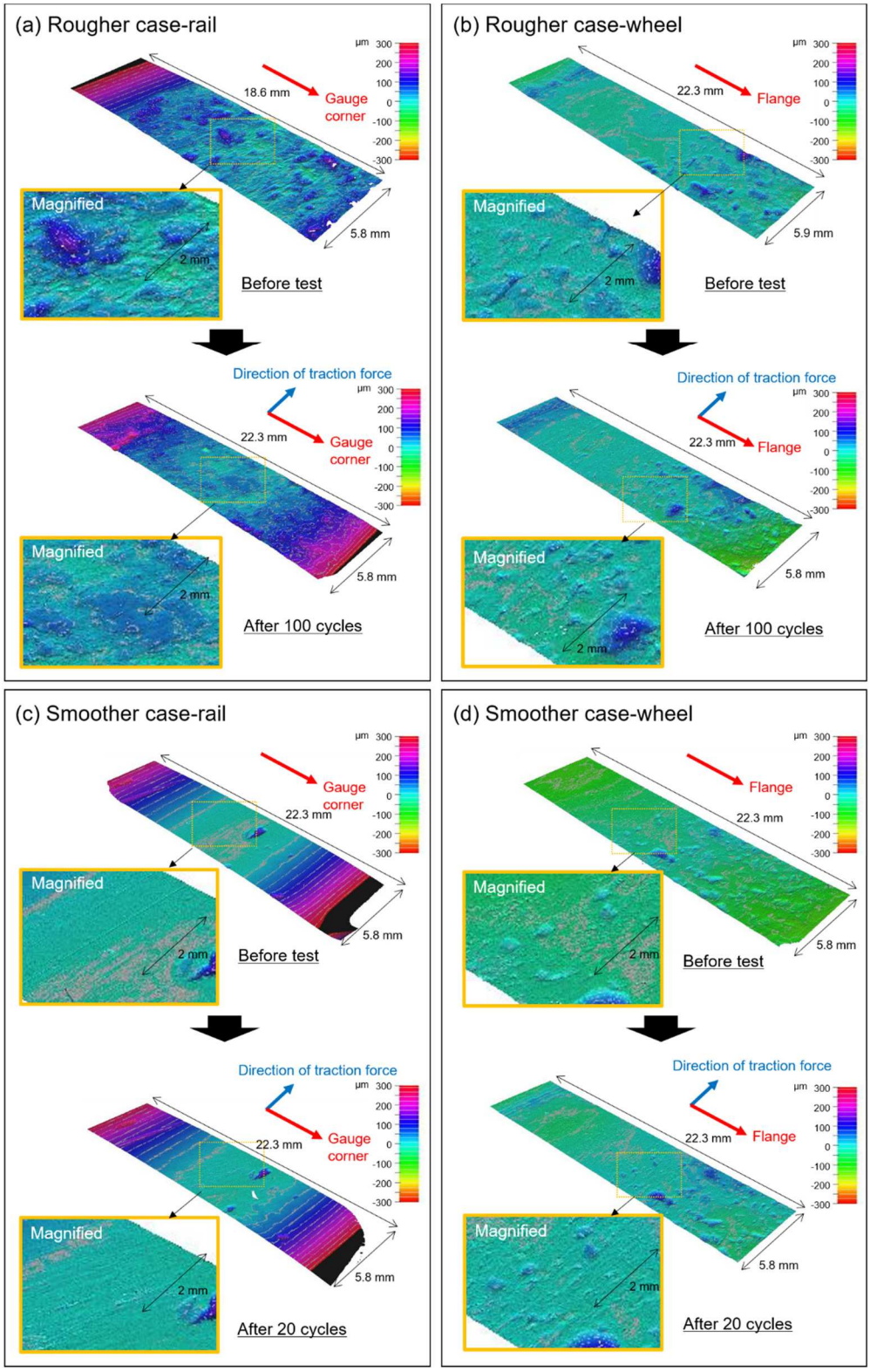

Figure 10. Comparison of the surface topography between before and after test cycles, (a) Rougher case-rail, (b) Rougher case-wheel, (c) Smoother case-rail, (d) Smoother case-wheel.

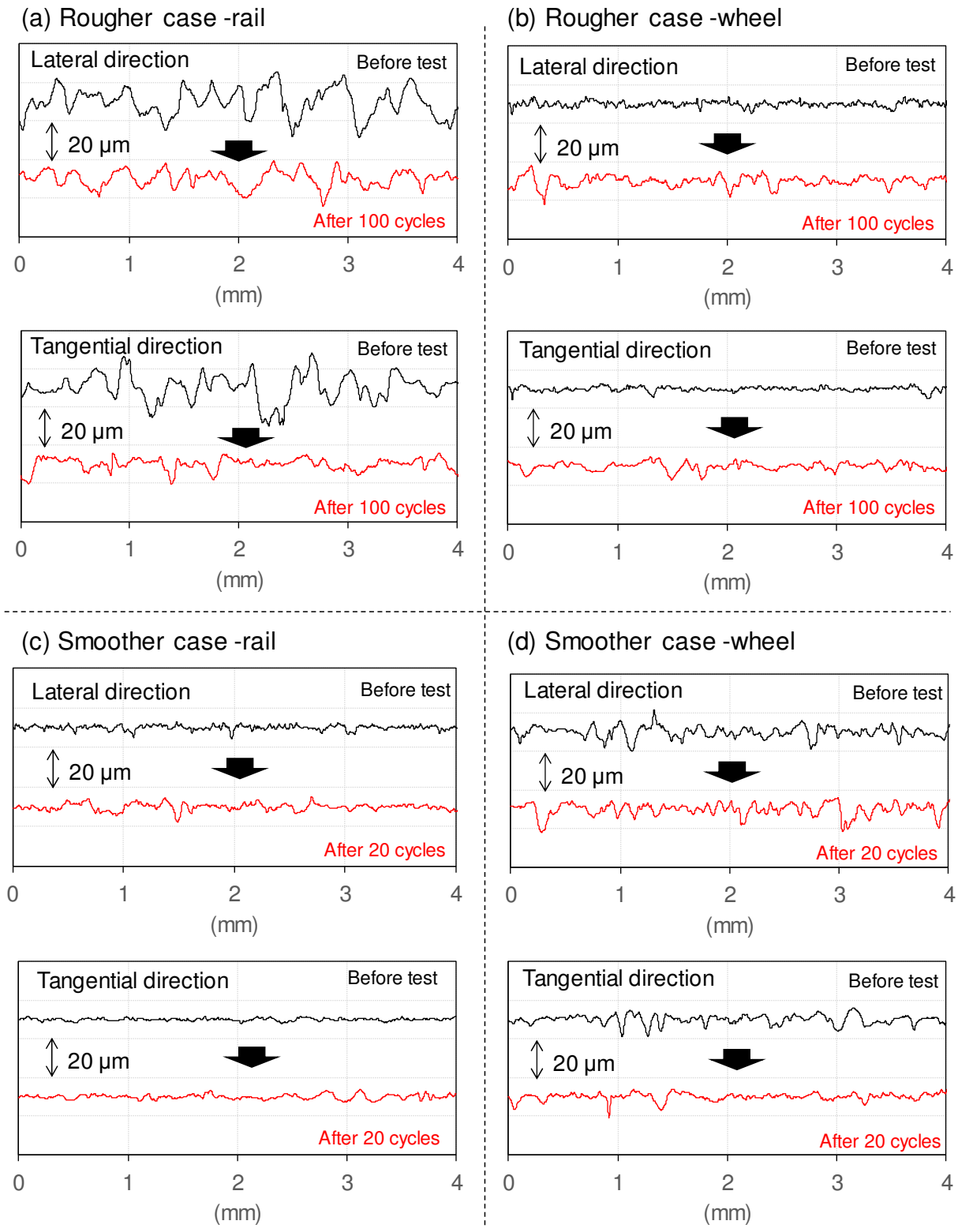

Figure 11. Comparison of the profiles before and after test cycles, (a) Rougher case-rail, (b) Rougher case-wheel, (c) Smoother case-rail, (d) Smoother case-wheel.

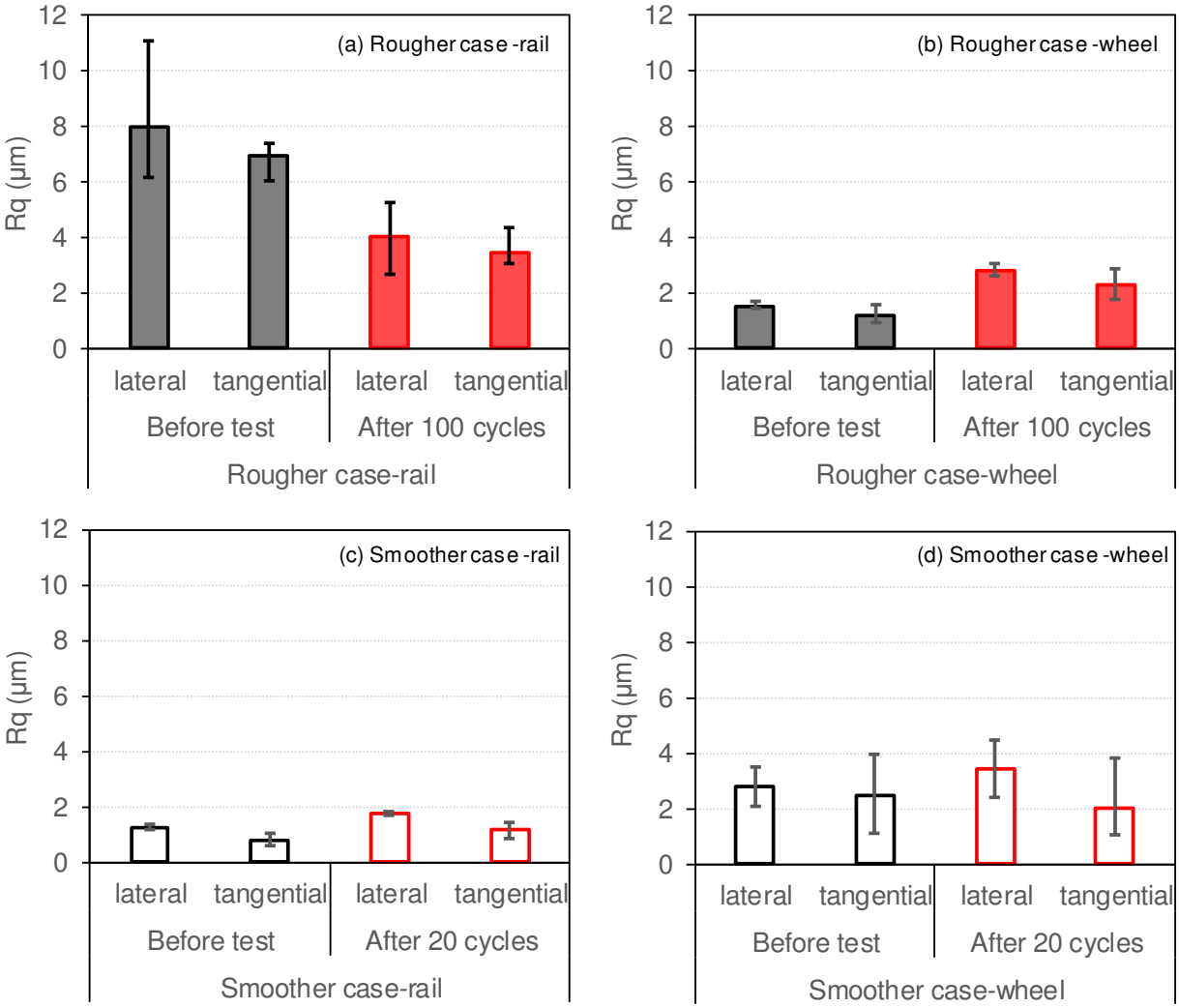

Figure 12. Comparison of the root-mean-square roughness, (a) Rougher case-rail, (b) Rougher case-wheel, (c) Smoother case-rail, (d) Smoother case-wheel.

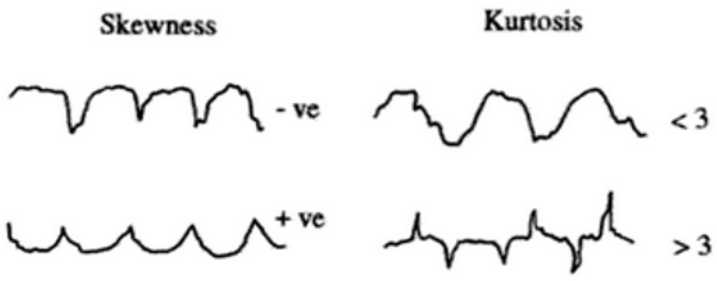

Figure 13. Schematic illustration for surface topography with various skewness and kurtosis [30].

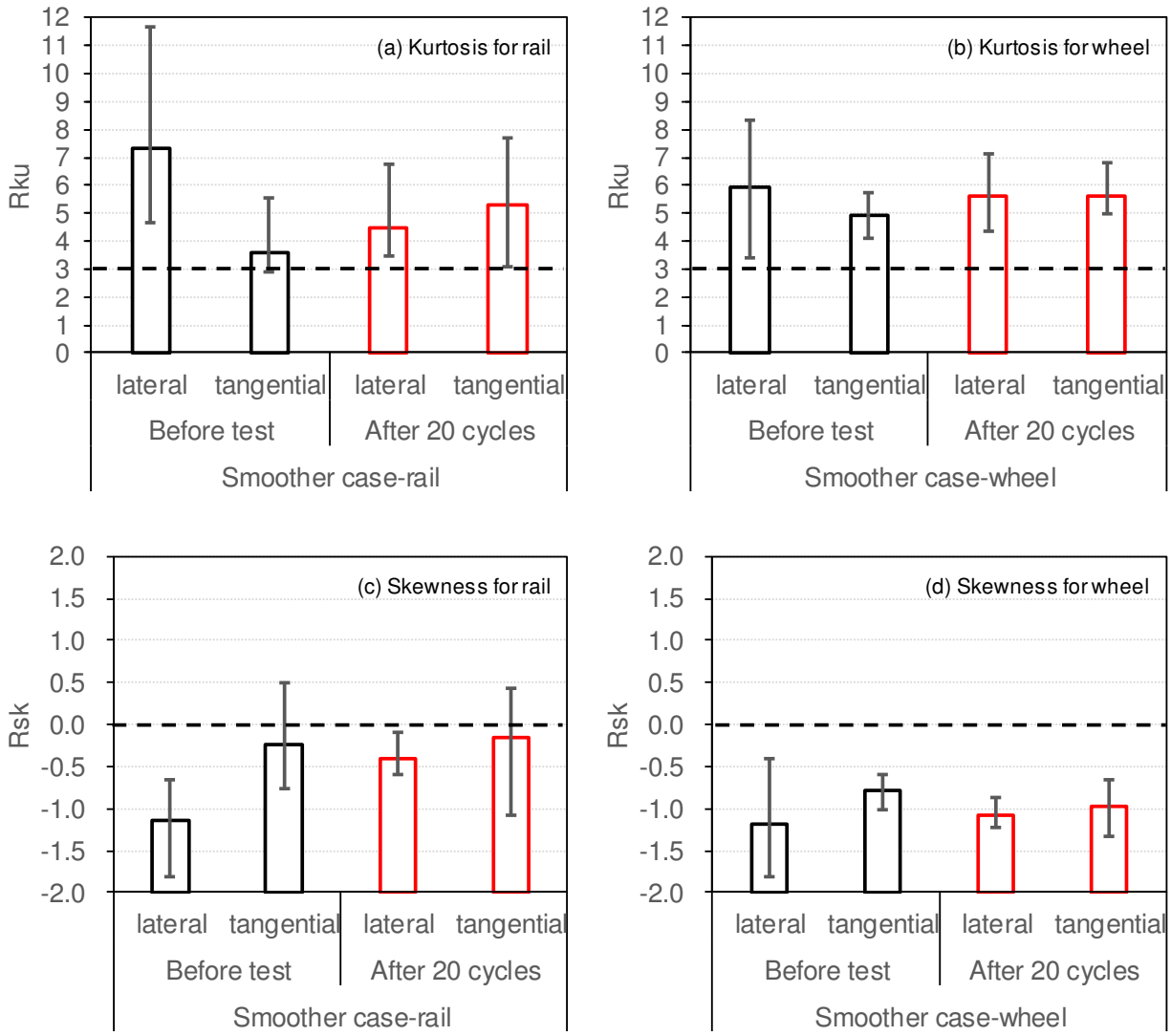

Figure 14. Comparison of the parameters of roughness in smoother case, (a)Kurtosis for rail, (b)Kurtosis for wheel, (c) Skewness for rail, (d) Skewness for wheel.

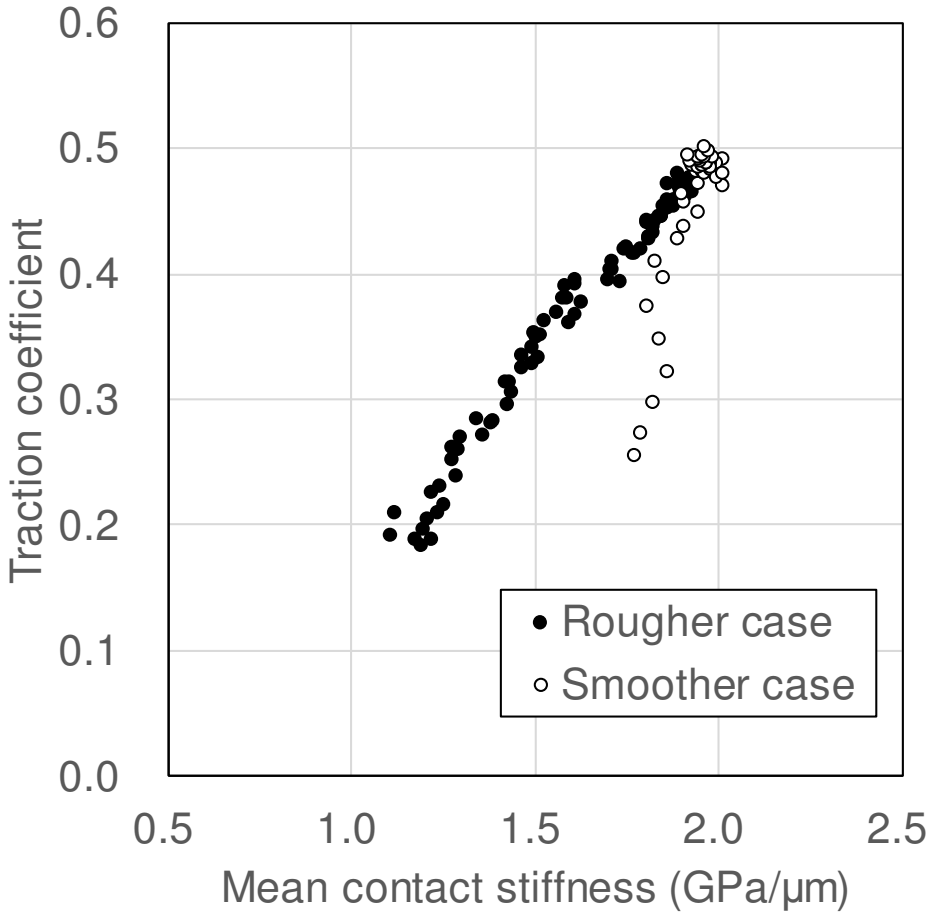

Figure 15. Relationship between mean contact stiffness and traction coefficient.

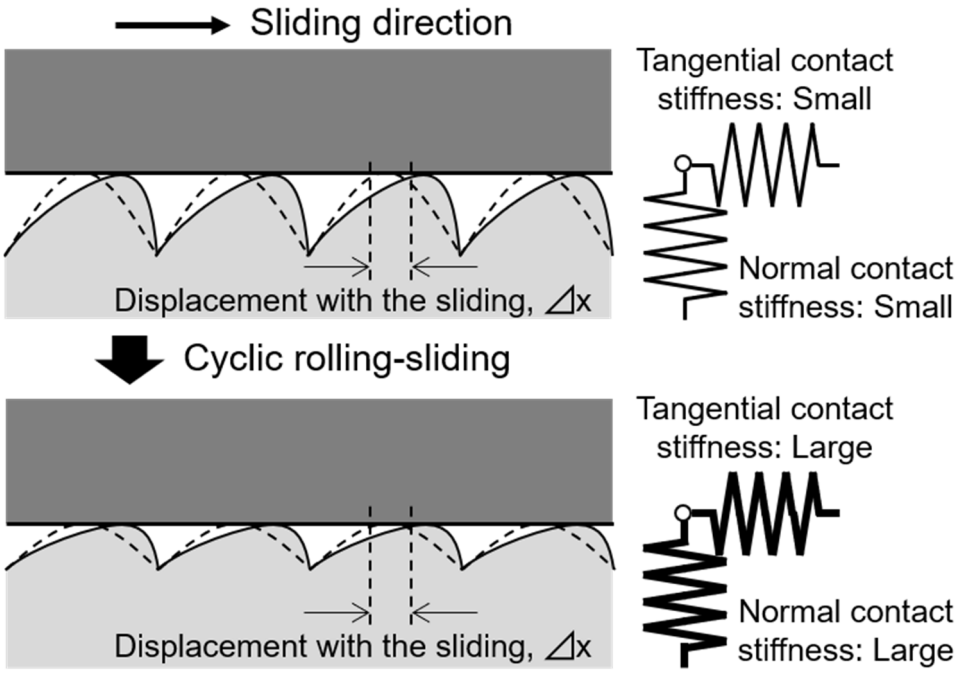

Figure 16. Schematic model of the transition of surface roughness and contact stiffness.

List of Tables

Table 1: Initial roughness (root-mean-square roughness) of test rail and wheel.

Case	Roughness, Rq (μm)			
	Rail		Wheel	
	Lateral direction	Tangential direction	Lateral direction	Tangential direction
Rougher case	8.0	6.9	1.5	1.2
Smoother case	1.2	0.8	2.8	2.4

Table 2: Test conditions.

Normal force (kN)	Slip ratio (%)	Velocity (mm/s)	Cycles for the measurement of traction coefficient and reflection coefficient (cycles)	Timing for replicating the surface topography (cycles)
80	3	10 for measure ment	1-10, 13-20, 23-30, 33-40, 43-50, 53-60 (63-100, only in rougher case)	After 100 (rougher case) After 20 (smoother case)